



## Research article

## Control of the selective adsorption of nitrate by the regional Lewis acid–base sites for improvement in the photocatalytic denitrification

Lifang Chen <sup>a,b</sup>, Haiyang Zheng <sup>b</sup>, Yibo Lu <sup>c</sup>, Xin Qiu <sup>b</sup>, Lian Wang <sup>b</sup>, Aimin Li <sup>a,b,\*</sup><sup>a</sup> State Key Laboratory of Pollution Control and Resource Reuse, School of Environment, Nanjing University, Nanjing, 210023, China<sup>b</sup> Nanjing University & Yancheng Academy of Environmental Protection Technology and Engineering, Yancheng, 224000, China<sup>c</sup> School of Agriculture and Biology, Shanghai Jiao Tong University, Shanghai, 200240, China

## ARTICLE INFO

## ABSTRACT

**Keywords:**  
 Photocatalytic  
 Nitrate reduction  
 Lewis acid–base sites  
 Selective adsorption

Photocatalytic denitrification is considered an environmentally friendly technology for reducing nitrate pollution. The construction of photocatalysts with high photocatalytic activity and excellent  $\text{NO}_3^-$  adsorption capacity to achieve high  $\text{N}_2$  selectivity remains challenging. In this work, hollow  $\text{SiO}_2/\text{SrTiO}_3/\text{TiO}_2$  photocatalysts were constructed, and unique element dopants were introduced into  $\text{SiO}_2$  and  $\text{SrTiO}_3$  to promote photocatalytic denitrification. Within 75 min, the nitrate removal rate and  $\text{N}_2$  selectivity of  $\text{Si}_{1-x}\text{Sr}_x\text{O}_2/\text{SrFe}_{0.06}\text{Ti}_{0.94}\text{O}_3/\text{TiO}_2$  were 95.82 % and 96.06 % respectively. After the same batch of  $\text{Si}_{1-x}\text{Sr}_x\text{O}_2/\text{SrFe}_{0.06}\text{Ti}_{0.94}\text{O}_3/\text{TiO}_2$  underwent five consecutive photocatalytic experiments, it still maintained a high photocatalytic denitrification efficiency (92.99 %). The analysis revealed that  $\text{SiO}_2$  enhanced the photocatalytic activity of the material by improving light capture. Furthermore, Lewis basic sites could be introduced by means of converting amorphous  $\text{SiO}_2$  to cristobalite through  $\text{Sr}^{2+}$  doping. Doping Fe into  $\text{SrTiO}_3$  could introduce strong Lewis acid sites. Unique regional Lewis acid–base sites regulated the selective adsorption of nitrate and improved the nitrate removal rate and  $\text{N}_2$  selectivity. This work provides new methods for photocatalytic nitrate reduction.

## 1. Introduction

The relatively high concentration of nitrate in water can pose potential threats to humans (Luo et al., 2023; Lee et al., 2021; Yu et al., 2024). An increase in the nitrate levels in natural water bodies intensifies eutrophication, leading to further deterioration of water quality (Shi et al., 2022). Nitrates may also be converted into dangerous substances such as nitrates in the human body, which can increase the risk of cancer (Jiang et al., 2022; Zhou et al., 2021). Therefore, exploring effective and environmentally friendly methods to alleviate nitrate pollution is highly important.

Photocatalytic reduction is considered an environmentally friendly technology for mitigating nitrate pollution (Li et al., 2022a; Zhao et al., 2018; Liu et al., 2016a). The photoreduction of nitrate in water to  $\text{N}_2$  primarily occurs through two pathways (Yang et al., 2022): i: Direct reduction process. Under illumination, the conduction band of the photocatalyst generates electrons, which can directly reduce  $\text{NO}_3^-$  adsorbed on the material's surface; ii: Indirect reduction process. Photogenerated holes in the valence band of the material react with formic acid and then form highly reductive  $\cdot\text{CO}_2$ , which can remove  $\text{NO}_3^-$  in the

solution. According to our previous research (Chen et al., 2024), the rate of nitrate conversion can be influenced by both direct and indirect reduction processes. However, under conditions where the photocatalyst has sufficient reductive ability, the selectivity for  $\text{N}_2$  is more significantly affected by the direct reduction process. Therefore, photocatalysts with high photocatalytic activity and good  $\text{NO}_3^-$  adsorption capacity are needed for achieving efficient nitrate conversion to  $\text{N}_2$ .

Because of its suitable valence band potential,  $\text{SrTiO}_3$  has drawn extensive research interest within the fields of photocatalysis (Grabowska, 2016; Cakra Wardhana et al., 2020). The formation of S-scheme heterojunctions between  $\text{SrTiO}_3$  ( $\text{ECB} \approx -1.5$ ,  $\text{EVB} \approx 1.6$ ) and  $\text{TiO}_2$  ( $\text{ECB} \approx -0.5$ ,  $\text{EVB} \approx 2.9$ ) effectively enhances the redox performance of the photocatalyst (Lei et al., 2024; Bashiri et al., 2021; Xu et al., 2020). Therefore,  $\text{SrTiO}_3/\text{TiO}_2$  is a promising candidate photocatalyst. Another important parameter for evaluating photocatalysts is the light-harvesting ability (Xiao et al., 2019; Liu et al., 2024). Light-scattering materials (LSMs, such as  $\text{SiO}_2$  and  $\text{Al}_2\text{O}_3$ ) are widely used in dye-sensitized solar cells to increase light harvesting (Bonyad-Shekalgorabi and Shariatinia, 2024; Sulaiman, 2021). LSMs can trap scattered light within the lattice through light confinement and

\* Corresponding author. State Key Laboratory of Pollution Control and Resource Reuse, School of Environment, Nanjing University, Nanjing, 210023, China.  
 E-mail address: liaimingroup@nju.edu.cn (A. Li).

increase the path of light absorption through scattering (Tong et al., 2017; Saito et al., 2017). When the LSMs have significantly different refractive index from that of the base material, this effect can be further strengthened at the doping interface (Hou et al., 2021; Son et al., 2013). Since the refractive indices of  $\text{SiO}_2$  ( $n = 1.55$ ) and  $\text{TiO}_2$  ( $n = 2.49$ ) differ significantly, (Hou et al., 2021); (Jain and El-Sayed, 2008) the construction of a  $\text{SiO}_2/\text{SrTiO}_3/\text{TiO}_2$  photocatalyst is expected to enhance light absorption.

Furthermore, enhancing the adsorption capacity of a material for nitrate helps achieve high  $\text{N}_2$  selectivity. (Chen et al., 2024); (Hou et al., 2018) As  $\text{NO}_3^-$  has the properties of a Lewis base, introducing Lewis acid sites can facilitate its adsorption (Li et al., 2022b; Yuan et al., 2013). For the  $\text{SrTiO}_3/\text{TiO}_2$  photocatalysts,  $\text{SrTiO}_3$  is the main active component and affects the direct reduction process. The method of introducing a strong Lewis acid by replacing  $\text{Ti}^{4+}$  in  $\text{SrTiO}_3$  with  $\text{Fe}^{3+}$  in situ to enhance the selectivity for  $\text{N}_2$  has been proven to be effective.<sup>11</sup> In addition, amorphous  $\text{SiO}_2$  adsorbs  $\text{NO}_3^-$  due to its typical Lewis acidity (Boonpai et al., 2020).  $\text{SiO}_2$  is not an electron donor, and  $\text{NO}_3^-$  adsorbed on the  $\text{SiO}_2$  surface does not undergo a reduction reaction; this reaction would be disadvantageous to the direct reduction process. The local stretching of the metal-oxygen bonds caused by the introduction of larger ions into the crystal may produce Lewis basic sites (Yang et al., 2024). Since like charges repel each other, the introduction of large metal ions into the crystalline structure of  $\text{SiO}_2$  may repel  $\text{NO}_3^-$ ; this would be beneficial to the direct reduction process. Alkaline earth metals are ideal doping elements since their ionic radii are usually larger than those of Si ions; on the other hand, alkaline earth metals can enter the amorphous  $\text{SiO}_2$  lattice through impregnation and serve as a melting aid to lower the crystallization temperature of  $\text{SiO}_2$  into cristobalite (Drisko et al., 2015).

Based on the above research background and analysis, in this study, the hollow spheres of  $\text{SiO}_2/\text{SrTiO}_3/\text{TiO}_2$  were fabricated and specifically doped with  $\text{SrTiO}_3$  and  $\text{SiO}_2$ . The analysis revealed that  $\text{SiO}_2$  enhanced the photocatalytic activity of the photocatalyst by improving light capture, promoting the direct reduction process. Additionally, the doping of Fe introduced strong Lewis acidic adsorption sites in  $\text{SrTiO}_3$ . Moreover, when  $\text{Sr}^{2+}$  was doped and  $\text{SiO}_2$  was converted into cristobalite. Lewis basic sites were introduced. The unique distribution of the Lewis acid-base sites promoted the selective adsorption of  $\text{NO}_3^-$  on  $\text{SrTiO}_3$ , improving the nitrate removal rate and  $\text{N}_2$  selectivity in the denitrification process. The aim of this work was to explore the influences of light scattering mechanisms and selective adsorption mechanisms on the photocatalytic denitrification process.

## 2. Materials and methods

### 2.1. Chemicals and materials

Titanium butoxide (TBOT, ≥99.5 %), tetraethyl orthosilicate (TEOS, ≥99 %), ammonium hydroxide solution (25 %–28 %),  $\text{Fe}(\text{NO}_3)_3 \cdot 9\text{H}_2\text{O}$  (99.9 %),  $\text{SrCl}_2 \cdot 6\text{H}_2\text{O}$  (99.5 %),  $\text{NaOH}$  (≥98 %) and hexadecyl trimethyl ammonium bromide (CTAB, ≥99 %) were provided by Macklin, Inc. Ethanol (99.7 %),  $\text{KNO}_3$  (≥99 %) and  $\text{Sr}(\text{OH})_2 \cdot 8\text{H}_2\text{O}$  (99.5 %) were provided by Aladdin Industrial, Inc.

### 2.2. Characterization

High-resolution transmission electron microscopy (HRTEM, JEOL JEM-2100F) and an energy dispersive spectrometer (EDS, X-MaxN 80T IE250) were used to characterize the morphology and microstructure of the catalyst. X-ray diffraction (XRD, X'Pert3 Powder) was used to test the crystal structure under the condition that the  $\text{Cu K}\alpha$  radiation range was from  $20^\circ$  to  $80^\circ$  (20). Ultraviolet-visible diffuse reflectance spectroscopy (UV-Vis DRS, lambda 1050) was used to measure the ultraviolet absorption curve of the catalyst. The chemisorption analyzer (AutoChem 2920-hiden HPR20) was employed for  $\text{NH}_3$ -TPD and  $\text{CO}_2$ -

TPD tests to reveal the Lewis acid-base site distribution on the catalyst surface. Test Procedure: The photocatalyst was continuously adsorbed using a 10 %  $\text{CO}_2$ –90 % He gas mixture (with a flow rate of 30 mL/min) at  $100^\circ\text{C}$  until the baseline was stable. Subsequently, in a He (flow rate of 30 mL/min) atmosphere, the temperature was raised to  $800^\circ\text{C}$  at a heating rate of  $10^\circ\text{C}/\text{min}$ , and the data were recorded. With 5,5-dimethyl-1-pyrroline N-oxide as the trapping agent,  $\cdot\text{O}_2^-$  formation was detected by electron spin resonance (ESR, Bruker A300). With an Ag/AgCl electrode as the reference, electrochemical workstation (CHI 760E) was employed to test the electrochemical impedance spectroscopy (EIS), transient photocurrent response (TPR), and Mott-Schottky curves of the materials.

### 2.3. Preparation of the $\text{TiO}_2$ hollow spheres

The preparation of  $\text{TiO}_2$  hollow spheres was achieved through etching  $\text{SiO}_2@\text{TiO}_2$ .

**Preparation of the  $\text{SiO}_2$  spheres:**  $\text{SiO}_2$  spheres were prepared using the modified Stober method. 12 mL of deionized water, 22 mL of ammonia water and 266 mL of ethanol were uniformly mixed and then stored at  $30^\circ\text{C}$ . Subsequently, a 0.5 mol/L ethanol solution of tetraethyl orthosilicate (TEOS) was added at an addition flow rate of 12 mL/h. After 4 h, the product was filtered out and rinsed with ethanol three times. Then it was dried at  $60^\circ\text{C}$  for 12 h to remove the excess solvent.

**Preparation of the  $\text{SiO}_2@\text{TiO}_2$  spheres:** Slowly add 2.127 g of tetrabutyl titanate into the mixed solution of 0.5 g of  $\text{SiO}_2$ , 0.6 mL of ammonium hydroxide and 120 mL of ethanol, and stir the mixture at  $45^\circ\text{C}$  for 40 h. Then calcine the separated powder at  $550^\circ\text{C}$  for 4 h.

**Preparation of the  $\text{TiO}_2$  hollow spheres:** 0.5 g of  $\text{SiO}_2@\text{TiO}_2$  was dispersed in 100 mL of deionized water. Then 0.5 g of  $\text{NaOH}$  was added and the mixture was kept in an oven at  $65^\circ\text{C}$  for 6 h. After that, the separated powder was dried at  $60^\circ\text{C}$  for 12 h to remove the excess water.

### 2.4. Preparation of $\text{SrTiO}_3/\text{TiO}_2$

Typically, at room temperature, 0.5 g of  $\text{TiO}_2$  hollow spheres, 0.83 g of  $\text{Sr}(\text{OH})_2 \cdot \text{H}_2\text{O}$  and 80 mL of deionized water were mixed and stirred for 1 h in a 100 ml Teflon-lined autoclave. Next, the suspension was kept at  $160^\circ\text{C}$  for 20 h. After the temperature dropped, the powder was separated and dried at  $60^\circ\text{C}$  for 12 h to remove the excess moisture, and  $\text{SrTiO}_3/\text{TiO}_2$  (ST) hollow spheres were obtained. Under the same conditions, a certain amount of  $\text{Fe}(\text{NO}_3)_3 \cdot 9\text{H}_2\text{O}$  was simultaneously added with  $\text{Sr}(\text{OH})_2 \cdot \text{H}_2\text{O}$  to the solution, and the  $\text{SrFe}_x\text{Ti}_{1-x}\text{O}_3/\text{TiO}_2$  (SFT) hollow spheres were obtained.

### 2.5. Preparation of $\text{SiO}_2/\text{SrTiO}_3/\text{TiO}_2$

**Preparation of  $\text{SiO}_2/\text{SrTiO}_3/\text{TiO}_2$  ( $\text{SiO}_2$  with an amorphous structure):** At room temperature, 0.5 g of CTAB and 0.3 g of ST or SFT were dispersed in 50 mL of deionized water. Then, they were stirred for 10 h. Subsequently, the powder was separated and rinsed with water and ethanol three times to remove the unadsorbed CTAB. The CTAB-modified ST or SFT was dispersed in the mixed solution of 6 mL of deionized water, 11 mL of ammonium hydroxide and 133 mL of ethanol, and was continuously stirred at  $30^\circ\text{C}$ . Subsequently, 5.4 mL of an ethanol solution of TEOS (1.6 g/L) was added to the system within a 1 h period, and the reaction continued for another 0.5 h. Subsequently, the white powder was filtered out, rinsed with ethanol three times and then dried at  $60^\circ\text{C}$  for 12 h to remove the excess solvent. Thus,  $\text{SiO}_2/\text{SrTiO}_3/\text{TiO}_2$  (SST) or  $\text{SiO}_2/\text{SrFe}_y\text{Ti}_{1-y}\text{O}_3/\text{TiO}_2$  (SSFT) was obtained.

**Preparation of  $\text{SiO}_2/\text{SrTiO}_3/\text{TiO}_2$  (cristobalite structure  $\text{SiO}_2$ ):** 0.5 g of SST or SSFT was dispersed with 0.055 g of  $\text{SrCl}_2 \cdot 2\text{H}_2\text{O}$  (excess) in 2 mL of deionized water. After standing still for 3 h, the mixture was maintained at  $120^\circ\text{C}$  for 30 min to evaporate excess water. The dried mixture was calcined in air at  $850^\circ\text{C}$  for 5 h. After the temperature was gradually lowered to room temperature, deionized water was used to

rinse away the  $\text{Sr}^{2+}$  attached to the surface of the catalyst. Subsequently, it was dried at 60 °C for 12 h to remove the excess moisture. Thus,  $\text{Si}_x\text{Sr}_{1-x}\text{O}_2/\text{SrTiO}_3/\text{TiO}_2$  (SSST) or  $\text{Si}_x\text{Sr}_{1-x}\text{O}_2/\text{SrFe}_y\text{Ti}_{1-y}\text{O}_3/\text{TiO}_2$  (SSSFT) was obtained. According to the loading amount of  $\text{SiO}_2$ , the photocatalysts were named SSSFT-0.5 %, SSSFT-1 %, SSSFT-2 %, etc.

## 2.6. Photocatalytic experiments

A quartz tube with an interlayer volume of 300 mL (outer diameter of 7 cm and inner diameter of 5.5 cm) was used to carry out the photocatalytic experiment. A 600 W medium-pressure mercury lamp (the main wavelength is 365 nm) was placed in the center of the device as a light source, and the outer wall of the mercury lamp was approximately 1.8 cm away from the inner wall of the quartz interlayer. Before the photocatalytic experiment, 75 mg photocatalyst was dispersed in 300 mL of  $\text{KNO}_3$  solution and kept in the dark for 20 min in order to reach the adsorption-desorption equilibrium of nitrate. Subsequently, 0.29 mL of formic acid was added into the reaction system, and the photocatalytic reaction was performed by turning on the light source. The reaction solution was periodically extracted and filtered to remove powder materials. During the photocatalytic experiment, the reaction solution was periodically extracted, with an ultraviolet-visible spectrophotometer being used to determine the concentrations of  $\text{NO}_3^-$ ,  $\text{NO}_2^-$  and  $\text{NH}_4^+$  in the reaction solution. Generally, after adding hydrochloric acid and sulfamic acid into the solution to be tested, the content of  $\text{NO}_3^-$  could be quantitatively analyzed by measuring the difference in absorbance at

220 nm and 275 nm. After adding the chromogenic agent, the content of  $\text{NO}_2^-$  could be quantitatively analyzed at 540 nm. After adding Nessler's reagent, the content of  $\text{NH}_4^+$  was measured at 420 nm. Due to the very low contents of NO and  $\text{N}_2\text{O}$  in the experiment, the nitrogen product balance equations (1) and (2) were employed in this work for calculating the nitrate removal rate ( $R_{\text{NO}_3^-}$ ) and  $\text{N}_2$  selectivity ( $S_{\text{N}_2}$ ).

$$R_{\text{NO}_3^-} = \frac{[\text{NO}_3^-]_0 - [\text{NO}_3^-]_t}{[\text{NO}_3^-]_0} \times 100 \% \quad (1)$$

$$S_{\text{N}_2} = \frac{[\text{NO}_3^-]_0 - [\text{NO}_3^-]_t - [\text{NO}_2^-]_t - [\text{NH}_4^+]_t}{[\text{NO}_3^-]_0 - [\text{NO}_3^-]_t} \times 100 \% \quad (2)$$

## 3. Results and discussion

The preparation process of the  $\text{Si}_x\text{Sr}_{1-x}\text{O}_2/\text{SrFe}_y\text{Ti}_{1-y}\text{O}_3/\text{TiO}_2$  (SSSFT) hollow spheres is shown in Fig. 1a. The modified Stöber method was used to obtain  $\text{SiO}_2$  spheres with smooth surfaces and uniform diameters (Fig. 1b). The hydrolysis product of TBOT was then coated on the  $\text{SiO}_2$  spheres and calcined in air at 550 °C for 4 h to obtain  $\text{TiO}_2@\text{SiO}_2$  (Fig. 1c). The  $\text{TiO}_2$  hollow spheres with a thickness of 40 nm were formed by etching  $\text{TiO}_2@\text{SiO}_2$  in a hot alkaline solution (Fig. 1d).  $\text{SrFe}_{0.06}\text{Ti}_{0.94}\text{O}_3/\text{TiO}_2$  (SFT) hollow spheres (Fig. 1e) and  $\text{SrTiO}_3/\text{TiO}_2$  (ST) hollow spheres (Fig. S1) formed during the hydrothermal reaction. The  $\text{SiO}_2$  particles were loaded onto SFT by hydrolysis to form  $\text{SiO}_2/\text{SrFe}_y\text{Ti}_{1-y}\text{O}_3/\text{TiO}_2$  (SSFT). Finally, in the presence of  $\text{Sr}^{2+}$ ,  $\text{SiO}_2$  was

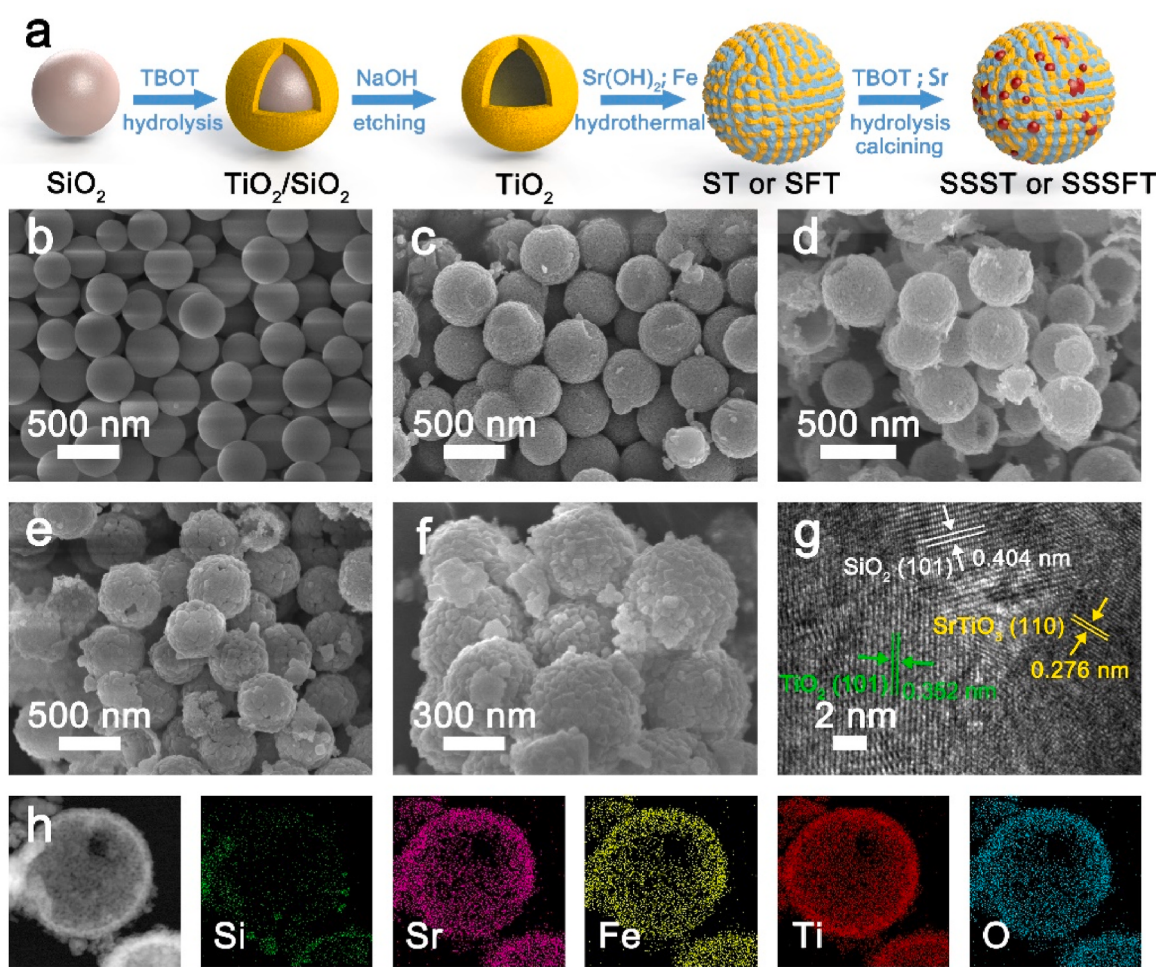


**Fig. 1.** (a) Schematic of the preparation of the SSSFT composite; SEM images of  $\text{SiO}_2$  (b),  $\text{TiO}_2@\text{SiO}_2$  (c),  $\text{TiO}_2$  hollow spheres (d), SFT hollow spheres (e) and SSSFT hollow spheres (f); (g)HRTEM images of SSSFT-1 %; (h) EDS elemental mappings of SSSFT-1 %.

converted into a cristobalite structure to produce  $\text{Si}_{1-x}\text{Sr}_x\text{O}_2/\text{SrFe}_y\text{Ti}_{1-y}\text{O}_3/\text{TiO}_2$  (SSSFT) at 850 °C (Fig. 1f). The HRTEM image (Fig. 1g) revealed two distinct lattice fringes. The lattice fringe with a spacing of 0.352 nm was attributed to the (101) plane of anatase  $\text{TiO}_2$ , while the one with a spacing of 0.276 nm was ascribed to the (110) plane of  $\text{SrTiO}_3$ , while the one with a spacing of 0.404 nm was ascribed to the (101) plane of  $\text{SiO}_2$ . EDS mapping (Fig. 1d) showed the distribution of Si, Sr, Fe, Ti and O, indicating that  $\text{SiO}_2$  was dispersed on  $\text{SrTiO}_3/\text{TiO}_2$  in the form of particles.

The crystal structure of the samples was characterized by XRD. SSFT-1 % did not show a significant signal in the XRD pattern; therefore, SSFT-10 % and SSSFT-10 % were prepared to analyze the crystal structure of  $\text{SiO}_2$ . According to JCPDS files No. 35-0734 and No. 21-1272, SSFT indicated that  $\text{SrTiO}_3$  presented a cubic perovskite structure and  $\text{TiO}_2$  adopted an anatase structure. Moreover, SSFT-10 % displayed a hump around 21.984, whereas SSSFT-10 % exhibited a strong peak at 21.984. This demonstrated that  $\text{SiO}_2$  in SSFT-10 % was of an amorphous structure, while  $\text{SiO}_2$  in SSSFT-10 % was of a cristobalite structure (Fig. 2a). Moreover, the doping of Fe and Sr didn't lead to the appearance of impurity peaks on the XRD patterns. These results indicated that Fe and Sr did not form independent oxides and had good solubility in the photocatalyst (Xie et al., 2008). The main diffraction peak of  $\text{SrTiO}_3$  (110) is magnified in Fig. 2b; here, although the ionic sizes of  $\text{Fe}^{3+}$  (0.79 Å) and  $\text{Ti}^{4+}$  (0.75 Å) were similar, the introduction of Fe resulted in a shift in the 2θ value to the right. This phenomenon was likely caused by the substitution of Ti by Fe in a lower oxidation state, and charge compensation occurred through the formation of oxygen vacancies; this led to a decrease in the lattice constant (Wu et al., 2012; da Silva et al., 2014). In contrast, because the ionic size of Sr was much larger than that of Si, the main diffraction peak of cristobalite shifted to the left (Fig. 2c); this result was consistent with Bragg's law.

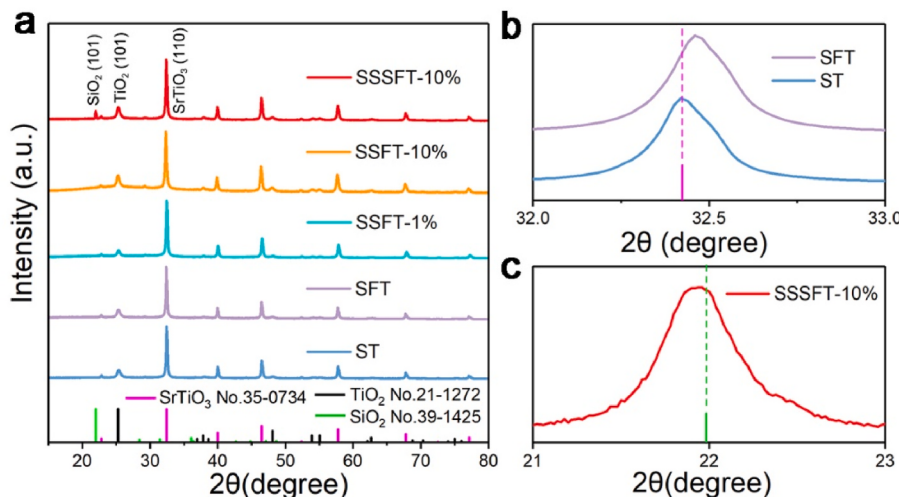
High-resolution XPS spectra (Fig. 3) were used to investigate the electronic states of Fe, Ti, O, and Si in SSSFT. Fig. 3a shows that there were two characteristic peaks of Fe 2p at 710.5 eV and 724.1 eV, which were assigned to  $\text{Fe } 2p_{3/2}$  and  $\text{Fe } 2p_{1/2}$ , respectively. The splitting energy of 13.6 eV and the peak intensity ratio of 1:2 indicated that the valence of Fe was +3. The high-resolution XPS spectrum of Ti 2p (Fig. 3b) exhibited characteristic peaks at 458.66 eV and 464.36 eV, which were assigned to  $\text{Ti } 2p_{3/2}$  and  $\text{Ti } 2p_{1/2}$ , respectively. Furthermore, the Ti 2p spectra of both SSSFT and SSFT (Fig. S2a) exhibited a 5.7 eV splitting energy, indicating Ti retained a +4 valence state during Fe doping. This suggests that after Fe doping, the photocatalyst compensated for negative charges by forming oxygen vacancies rather than by changing the

valence state of Ti (Chen et al., 2024). This was also confirmed by the high-resolution XPS spectrum of O 1s. The peak at 529.6 eV was attributed to the lattice oxygen of  $\text{SrTiO}_3$  and  $\text{TiO}_2$ , the peak at 530.9 eV was assigned to oxygen vacancies, and the peak at 532.4 eV was the lattice oxygen of  $\text{SiO}_2$  (Tang et al., 2014). In addition, the Si 2p XPS spectrum showed a characteristic peak at 103.2 eV, which was in good agreement with the XPS data of cristobalite reported by Shen et al., further indicating that the  $\text{SiO}_2$  in the photocatalyst had a cristobalite structure (Shen et al., 2011). Furthermore, the Si 2p spectrum (Fig. S2b) of SSFT exhibited a broad absorption peak, possibly indicating amorphous  $\text{SiO}_2$  in SSFT. Combined with XRD results, we attribute this to Sr doping converting amorphous  $\text{SiO}_2$  into cristobalite.

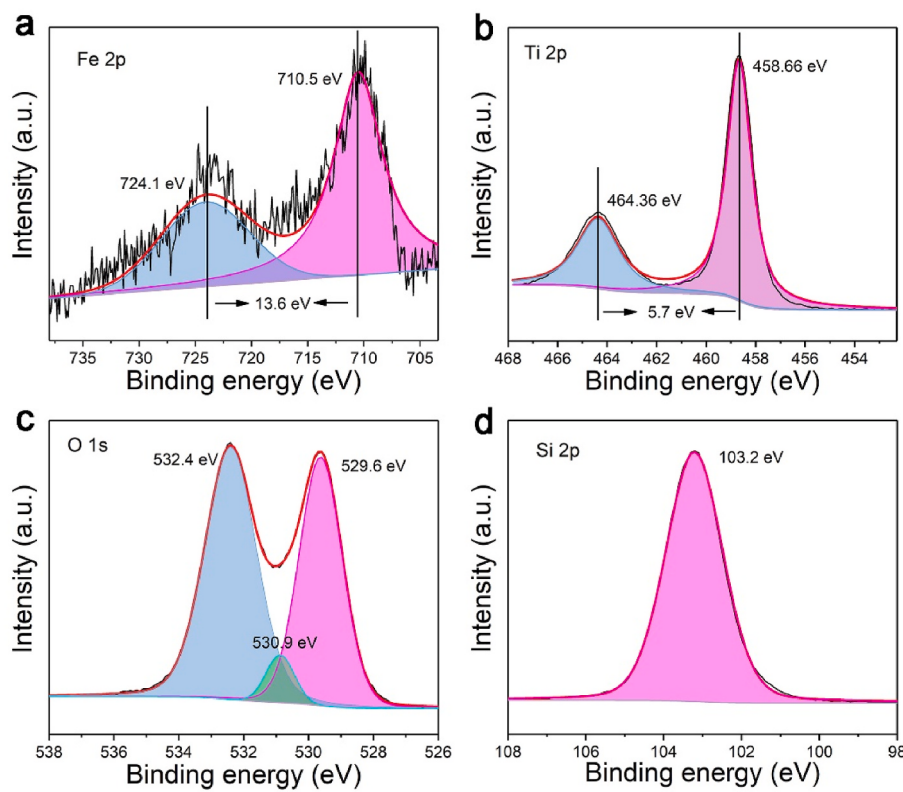
After adding 25 mmol/L formic acid into the photocatalytic reaction system, the photocatalytic denitrification performance of the photocatalyst was investigated at room temperature. Fig. S3 showed the standard curves of ion concentration-absorbance for  $\text{NO}_3^-$ ,  $\text{NO}_2^-$  and  $\text{NH}_4^+$ . Fig. 4a indicates that no significant  $\text{NO}_3^-$  reduction reaction occurred under the conditions of only formic acid and only light. As shown in Fig. 4a, the reduction rate of nitrate on ST was significantly greater than that on the individual oxide materials; these results indicated that the construction of the heterojunction improved the denitrification performance. As shown in Fig. 4a, loading 1 %  $\text{SiO}_2$  was beneficial for the reduction of nitrate, which was likely caused by the improvement in light capture by  $\text{SiO}_2$ . In addition, the doping of Fe within  $\text{SrTiO}_3$  and the doping of Sr within  $\text{SiO}_2$  could further improve the nitrate removal rate. In previous work, we reported that the introduction of strong Lewis acid adsorption sites by Fe promoted the direct reduction process and resulted in a faster reduction rate11. The incorporation of Sr could promote the reduction reaction of nitrate by reducing the ineffective adsorption of  $\text{NO}_3^-$  on  $\text{SiO}_2$  through the introduction of the basic sites.

Fig. 4b shows the content of nitrogen species and  $\text{N}_2$  selectivity in the reaction system after 75 min. As shown in Fig. 4b, compared with that of ST, the selectivity of  $\text{N}_2$  for SSSFT-1 % could be increased from 75.74 % to 96.06 %. Formula 2 shows that the residual amount of  $\text{NO}_3^-$  had no effect on  $\text{N}_2$  selectivity. Fig. 4b showed that the content of  $\text{NO}_2^-$  was always less than 2 %, indicating that the amount of  $\text{NO}_2^-$  generated had little impact on the selectivity of  $\text{N}_2$ . The amount of  $\text{NH}_4^+$  produced in Fig. 4b corresponded to the trend of the change in nitrogen gas selectivity. Therefore, the generation of  $\text{NH}_4^+$  played a decisive role in  $\text{N}_2$  selectivity. These findings indicated that Fe and cristobalite could influence  $\text{N}_2$  selectivity by regulating the generation of  $\text{NH}_4^+$ .

Figs. 4c and 3d presented the  $\text{NO}_3^-$  reduction rates and  $\text{N}_2$  selectivity



**Fig. 2.** (a) XRD pattern of samples; (b) The magnified XRD image of SFT and ST at the (110) crystal plane. (c) The magnified XRD image of SSSFT-10 % at the (101) crystal plane.



**Fig. 3.** High-resolution XPS images of (a) Fe 2p, (b) Ti 2p, (c) O 1s and (d) Si 2p for  $\text{Si}_x\text{Sr}_{1-x}\text{O}_2/\text{SrFe}_y\text{Ti}_{1-y}\text{O}_3/\text{TiO}_2$ .

under different initial formic acid contents. In Fig. 4c, it was shown that formic acid significantly promoted  $\text{NO}_3^-$  reduction. Formic acid with a concentration higher than 20 mmol/L could remove over 95 % of  $\text{NO}_3^-$  within 75 min. However, the higher production of  $\text{NH}_4^+$  led to the  $\text{N}_2$  selectivity at formic acid concentrations of 30 mmol/L and 40 mmol/L being lower than that at 20 mmol/L. According to our prior experience, this might be due to the fact that a higher formic acid concentration enhanced the indirect reduction process, which was unable to effectively control  $\text{NH}_4^+$  production. Moreover, based on mass balance, the removal of 100 mg N/L of nitrate through the indirect reduction process required approximately 40 mmol/L of formic acid. It was noteworthy that under the optimal conditions of this work, only 20 mmol/L of formic acid was needed to achieve a 96.06 % removal rate of nitrate. This phenomenon further verified that both the indirect and direct reduction processes were involved in the removal of  $\text{NO}_3^-$ , consequently reducing the formic acid consumption by approximately 50 %. The decrease in formic acid consumption was conducive to cost reduction and the prolongation of the photocatalyst's service life.

The performance decay rate was an important indicator for evaluating the performance of catalysts. The utilized SSSFT-1 % catalyst was rinsed thrice in deionized water and anhydrous ethanol, followed by drying and subsequent reuse in subsequent experiments. As shown in Fig. 4e, after five cycles of reuse, the conversion rate of  $\text{NO}_3^-$  on the SSSFT-1 % catalyst decreased from 95.82 % to 92.99 %. These results indicate that the catalyst has good stability. In addition, the XRD pattern of SSSFT-1 % remained nearly unchanged before and after the photocatalytic experiment (Fig. S4), further confirming its structural stability.

The band structure of the photocatalysts was analyzed via UV-vis DRS and Mott-Schottky measurements. As shown in Fig. 5a, the UV-vis DRS spectrum displayed strong optical absorption signal intensity for  $\text{SrTiO}_3/\text{TiO}_2$  in the ultraviolet spectral range. As shown in Fig. 5b, the band gaps of  $\text{SrTiO}_3$  and  $\text{TiO}_2$  were 3.01 eV and 3.29 eV, respectively. Fig. 5c indicated that the flat band positions of  $\text{SrTiO}_3$  and  $\text{TiO}_2$  relative to the standard hydrogen electrode (SHE) were  $-1.21 \text{ V}$  and  $-0.68 \text{ V}$ ,

respectively. Additionally, the positive slope of the Mott-Schottky curves indicated that both  $\text{SrTiO}_3$  and  $\text{TiO}_2$  were n-type semiconductors and that their conduction band edges (CB) were aligned with the flat band edges ( $E_{fb}$ ) (Wang et al., 2021; Liu et al., 2023). Therefore, the valence band potentials of  $\text{SrTiO}_3$  and  $\text{TiO}_2$  were 1.8 eV and 2.61 V respectively. EPR tests (depicted in Fig. 5d) were employed to facilitate the demonstration of the heterojunction type. Fig. 5d showed that the DMPO- $\text{O}_2^-$  signal intensity of the original  $\text{TiO}_2$  was weaker than that of  $\text{SrTiO}_3$ , perhaps because  $\text{SrTiO}_3$  had a higher CB potential. The slightly stronger DMPO- $\text{O}_2^-$  signal intensity of  $\text{SrTiO}_3/\text{TiO}_2$  than that of  $\text{SrTiO}_3$  indicated that  $\text{SrTiO}_3/\text{TiO}_2$  did not conform to the type-II heterojunction theory (Liu et al., 2016b). Additionally, the charge transfer ability of the photocatalysts was analyzed by EIS. Fig. S5 showed that  $\text{SrTiO}_3/\text{TiO}_2$  exhibited a smaller arc than other materials, indicating that it had the lowest charge transfer resistance. Extending these findings and those of previous studies, (Wang et al., 2021); (Zhang et al., 2023; Li et al., 2021) we believed that  $\text{SrTiO}_3/\text{TiO}_2$  was more in line with the characteristics of the S-scheme heterojunction.

$\text{SrTiO}_3/\text{TiO}_2$  with different amounts of  $\text{SiO}_2$  (amorphous) were prepared to explore the role of  $\text{SiO}_2$  in denitrification. As shown in Fig. 6a, the nitrate removal rate exhibited a trend of first increasing and then decreasing with increasing  $\text{SiO}_2$  content. The nitrate removal rate was beneficial in the presence of 0.5 % and 1 %  $\text{SiO}_2$ . The content of nitrogen species in the reaction system after 75 min (Fig. 6b) also initially increased and then decreased with increasing  $\text{N}_2$  selectivity. The  $\text{N}_2$  selectivity at less than 2 %  $\text{SiO}_2$  was superior to that of the original photocatalyst. To explain this phenomenon, UV-vis was used to probe the photoresponsive ability of the photocatalysts. As shown in Fig. 6c, the light absorption intensity of the photocatalysts in the ultraviolet band increased with increasing  $\text{SiO}_2$  content. Previous studies have indicated that the change in  $\text{N}_2$  selectivity is attributed mainly to the direct reduction process (Chen et al., 2024). Therefore, the improvement in the nitrate removal rate and  $\text{N}_2$  selectivity was potentially caused by the enhanced light capture; this enhancement increased the

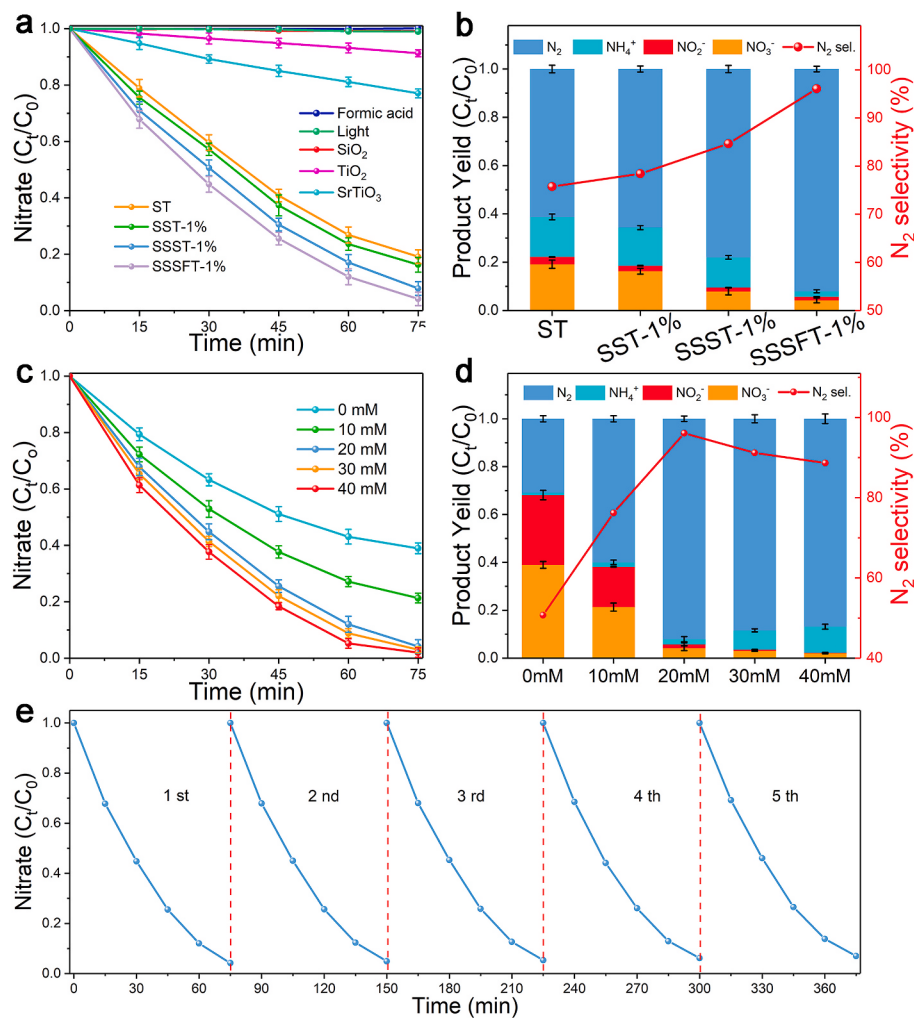


**Fig. 4.** (a) Nitrate removal rate for as-prepared samples and (b)  $\text{N}_2$  selectivity after 75 min; (c) Nitrate removal rate and (d)  $\text{N}_2$  selectivity after 90 min of SSSFT-1 % at different concentration of formic acid; (e) Successive photocatalytic experiments of SSSFT-1 %. In experiment: 300 ml solution treated, 0.345 g formic acid, 75 mg catalyst, reaction at 40 °C.

photocatalytic activity of the photocatalyst and promoted the direct reduction process. NH<sub>3</sub>-TPD was a characterization method for analyzing the distribution of acid sites on photocatalysts. Fig. 6d showed that the greater the SiO<sub>2</sub> loading amount, the stronger the NH<sub>3</sub>-TPD response signal, suggesting an increase in acid sites with the rise of SiO<sub>2</sub> loading. FTIR with pyridine adsorption characterized the types of acid sites on the material. The absorption peak at 1450 cm<sup>-1</sup> signified Lewis acid, and the one near 1540 cm<sup>-1</sup> denoted Brønsted acid. As Fig. S6 shows, for SFT and SSFT-1 %, the peaks related to Lewis acid were relatively intense, suggesting that Lewis acid was the dominant acid site type on the photocatalyst. The distribution of SiO<sub>2</sub> on SrTiO<sub>3</sub>/TiO<sub>2</sub>-5 % is shown in Fig. S7. As shown in Fig. S7, a high loading of SiO<sub>2</sub> can coat a significant amount of SrTiO<sub>3</sub>/TiO<sub>2</sub>, further hindering the effective adsorption of nitrate. Therefore, the photocatalysts with high SiO<sub>2</sub> loading showed lower conversion rates of nitrate and reduced N<sub>2</sub> selectivity.

CO<sub>2</sub>-TPD was used to investigate the changes in Lewis base sites on SiO<sub>2</sub>/SrTiO<sub>3</sub>/TiO<sub>2</sub> (SST) and Si<sub>1-x</sub>Sr<sub>x</sub>O<sub>2</sub>/SrTiO<sub>3</sub>/TiO<sub>2</sub> (SSST). As shown in Fig. 7a, more Lewis acid sites were observed on SSST. To explore the location of the Lewis base sites, Sr-SrTiO<sub>3</sub>/TiO<sub>2</sub> (Sr-ST) was prepared without SiO<sub>2</sub> using the same method. Fig. S8 showed that the signal intensities of Sr-SrTiO<sub>3</sub>/TiO<sub>2</sub> and SrTiO<sub>3</sub>/TiO<sub>2</sub> were close, confirming that the Lewis base sites were on SiO<sub>2</sub> rather than on SrTiO<sub>3</sub>/TiO<sub>2</sub>. Amorphous SiO<sub>2</sub> was converted to a cristobalite structure when Sr was present and weakened the ineffective adsorption of NO<sub>3</sub><sup>-</sup>. The conversion

rate of nitrate on SSST (Fig. 7b) was greater than that on SST with the same SiO<sub>2</sub> content (Fig. 6a). In addition, the doping of Sr slightly improved the N<sub>2</sub> selectivity (Fig. 7c), possibly because SiO<sub>2</sub> was not the active component that directly affected the reduction process. Different from SST, the denitrification efficiency of SSST-0.5 % was greater than that of SSST-0.5 %. This was likely caused by the repulsion of NO<sub>3</sub><sup>-</sup> adsorption by Lewis base sites, even if a small increase in SiO<sub>2</sub> loading did not have a significant adverse effect on nitrate reduction.

As previously reported, Fe doping into SrTiO<sub>3</sub> introduces abundant Lewis acid sites to promote NO<sub>3</sub><sup>-</sup> adsorption. The optimal doping concentration of 0.06 mol% exhibited superior denitrification efficiency, attributed to its lower charge transfer resistance and higher photocurrent intensity. Therefore, 0.06 mol% Fe was doped into SrTiO<sub>3</sub> to further modulate the selective adsorption of NO<sub>3</sub><sup>-</sup> (Chen et al., 2024). NH<sub>3</sub>-TPD (Fig. 7d) showed a strong absorption peak near 650 nm in SSSFT-1 %. This was consistent with previous research results, indicating that the doping of Fe introduced strong Lewis acid sites. This was important for the adsorption of NO<sub>3</sub><sup>-</sup>. The results of the photocatalytic denitrification experiments confirmed this point since the doping of 0.06 % Fe further improved the conversion rate of nitrate (Fig. 7b) and N<sub>2</sub> selectivity (Fig. 7c).

Brunauer-Emmett-Teller (BET) measurements were performed to characterize catalyst specific surface areas, eliminating the influence of surface area variations on NO<sub>3</sub><sup>-</sup> adsorption. As shown in Table S1, increasing Si<sub>1-x</sub>Sr<sub>x</sub>O<sub>2</sub> loading proportionally enhanced photocatalyst

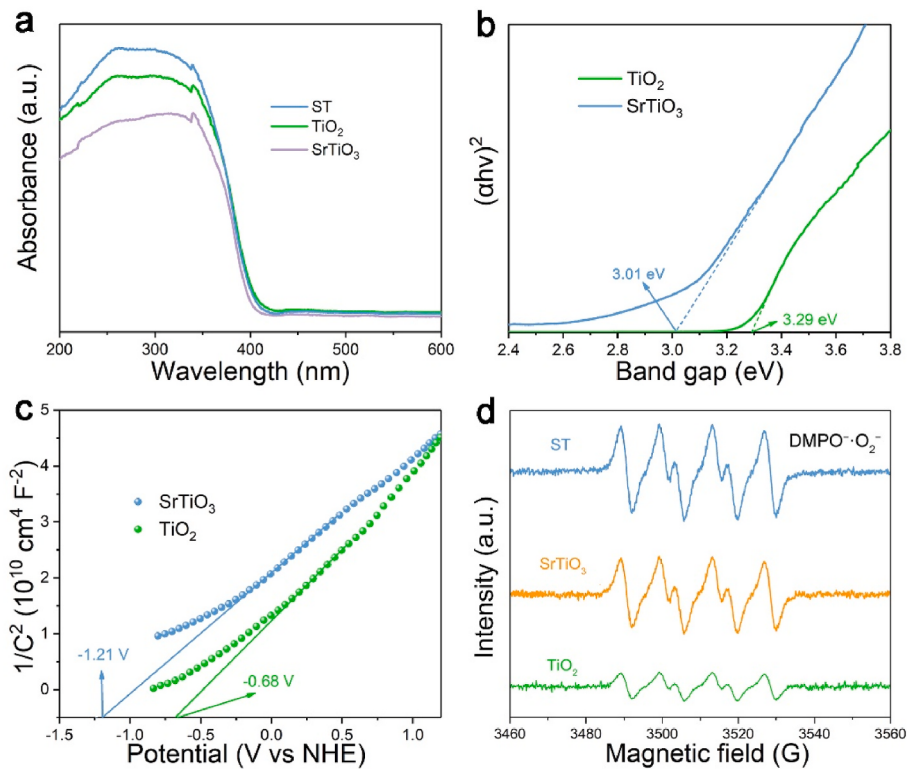


**Fig. 5.** (a) UV–vis spectra and (b) corresponding band gap energies of  $\text{SrTiO}_3$  and  $\text{TiO}_2$ ; (c) Mott–Schottky plot of  $\text{SrTiO}_3$  and  $\text{TiO}_2$ ; (d) DMPO– $\text{O}_2^-$  adducts over  $\text{TiO}_2$ ,  $\text{SrTiO}_3$ , and ST under illumination for 15 min.

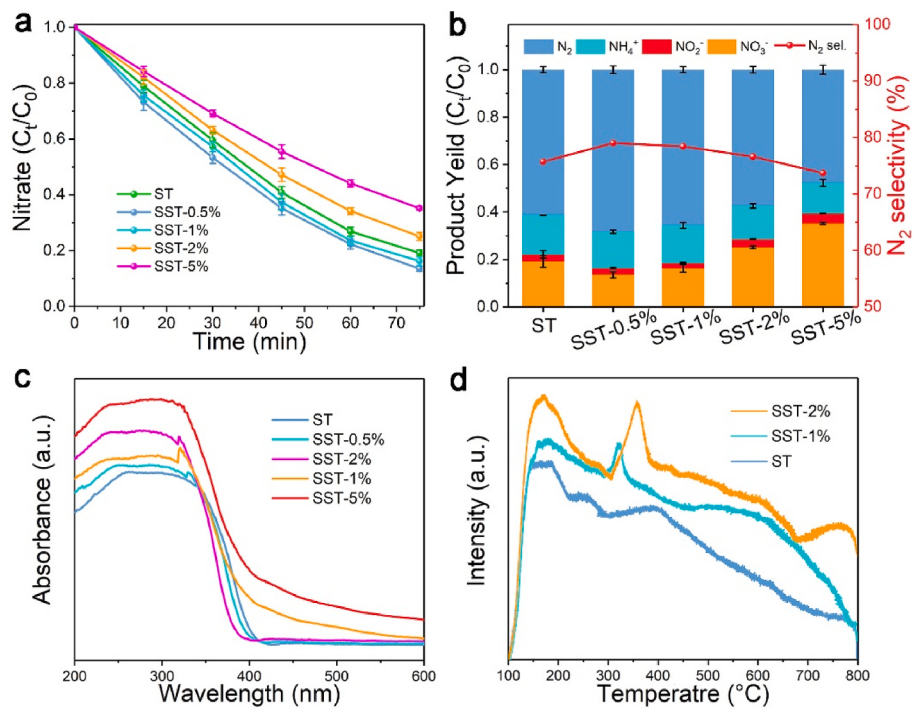


**Fig. 6.** Nitrate removal rate (a),  $\text{N}_2$  selectivity after 75 min (b), UV–vis spectra (c) and  $\text{NH}_3$ -TPD plots (d) of SST with various amorphous  $\text{SiO}_2$  contents.

surface area. Notably, Sr-ST exhibited a surface area comparable to ST, indicating that the high-surface-area crystalline  $\text{SiO}_2$  dominates the overall surface area increase, while  $\text{SrTiO}_3$  contributes negligibly. Since  $\text{SiO}_2$  does not participate in reduction reactions, its increased surface area had minimal impact on denitrification. The similar specific surface

areas of SSST-1 % and SSSFT-1 % further validate that abundant Lewis acid sites are critical for boosting nitrate conversion and  $\text{N}_2$  selectivity.

For further elucidating the mechanism underlying the influence of regional Lewis acid-base sites on nitrate reduction, methyl viologen dichloride ( $\text{MV}^{2+}$ ) was incorporated into the reaction system as a

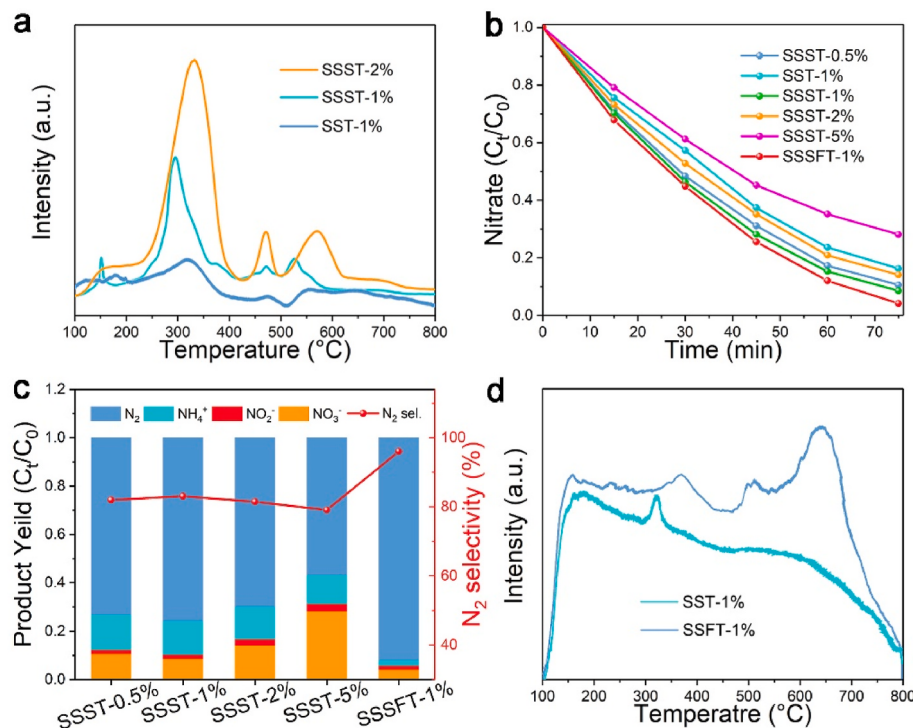


**Fig. 7.** CO<sub>2</sub>-TPD plots (a), nitrate removal rate (b) and N<sub>2</sub> selectivity after 75 min (c) of SSST with various cristobalite contents; (d) NH<sub>3</sub>-TPD plots of SST-1 % and SSFT-1 %.

quencher for ·CO<sub>2</sub> to suppress the indirect reduction process. (Chen et al., 2024); (Tang et al., 2019); (Xu et al., 2023) Fig. 8a and b demonstrated that SSSFT-1 % exhibited the optimal NO<sub>3</sub> reduction rate and N<sub>2</sub> selectivity, which was ascribed to the selective NO<sub>3</sub> adsorption by SSSFT-1 %, signifying the promotion of the direct reduction process by the regional Lewis acid-base sites. The NO<sub>3</sub><sup>-</sup> reduction rate of SST-1 % was inferior to that of ST, potentially attributable to the competitive adsorption of NO<sub>3</sub><sup>-</sup> on SiO<sub>2</sub>. Additionally, Fig. 8b illustrated that the N<sub>2</sub> selectivity of SST-1 % surpassed that of ST. Given the relatively high yield of NO<sub>2</sub> by ST, it indicated that SiO<sub>2</sub> augmented the reduction capacity of the catalyst. Fig. 8b further revealed that the concentration of NH<sub>4</sub><sup>+</sup> was substantially diminished compared to the scenario without the addition of MV<sup>2+</sup>, implying that the direct reduction process was inclined to produce N<sub>2</sub> instead of NH<sub>4</sub><sup>+</sup>, in accordance with our prior research findings. Therefore, we considered that the regional Lewis acid-base sites regulated the selective adsorption of NO<sub>3</sub><sup>-</sup>, thereby affecting the direct reduction process and enhancing the nitrate conversion rate and N<sub>2</sub> selectivity.

SSSFT-1 % demonstrated excellent photocatalytic denitrification performance under low formic acid dosage, indicating practical

advantages like reduced reagent costs and improved effluent quality. However, catalyst synthesis in this work involved complex procedures, hindering large-scale production. In future studies, we plan to use commercial precursors and streamline synthesis steps to simplify synthesis and enhance practical applicability.

#### 4. Conclusions

Herein, we propose an efficient hollow SiO<sub>2</sub>/SrTiO<sub>3</sub>/TiO<sub>2</sub> photocatalyst for photocatalytic denitrification. Studies have shown that the S-scheme heterojunction promotes photoinduced carrier separation and enhances the photocatalytic activity of the material. In our study, SiO<sub>2</sub> promoted the indirect reduction process by enhancing light capture. Furthermore, localized Lewis acid-base sites were designed on the photocatalyst. Amorphous SiO<sub>2</sub> was converted into a cristobalite structure at high temperatures under the doping of Sr<sup>2+</sup>. Based on our analysis, the presence of Sr increased the lattice constant of cristobalite, thereby introducing a large number of Lewis basic sites and reducing the ineffective adsorption of NO<sub>3</sub><sup>-</sup> on SiO<sub>2</sub>. In addition, the incorporation of Fe into the SrTiO<sub>3</sub> lattice could introduce strong Lewis acid sites and

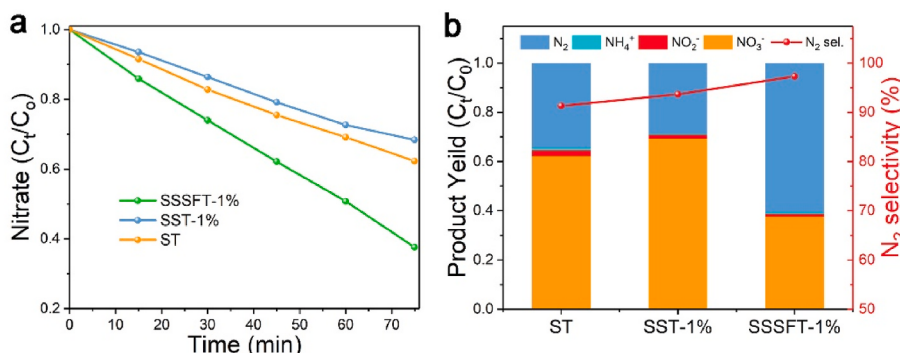


**Fig. 8.** (a) Nitrate removal rate (b) and N<sub>2</sub> selectivity after 75 min when MV<sup>2+</sup> was present.

improve the adsorption of  $\text{NO}_3^-$  on  $\text{SrTiO}_3$ . The unique distribution of Lewis acid–base sites regulated the selective adsorption of  $\text{NO}_3^-$  on the photocatalyst, thereby improving the conversion rate of nitrate and  $\text{N}_2$  selectivity in the denitrification process. Moreover, it reduced the formic acid dosage to approximately 50 % of the theoretical value. In this study, regional Lewis acid–base sites were designed for regulating the selective adsorption of nitrate, and our developed photocatalysts have potential applications in photocatalytic denitrification.

### CRediT authorship contribution statement

**Lifang Chen:** Writing – review & editing, Writing – original draft, Validation, Resources, Investigation, Funding acquisition, Conceptualization. **Haiyang Zheng:** Writing – original draft, Visualization, Investigation, Formal analysis, Data curation, Conceptualization. **Yibo Lu:** Validation, Data curation. **Xin Qiu:** Investigation, Conceptualization. **Lian Wang:** Validation, Methodology. **Aimin Li:** Writing – review & editing, Resources, Project administration, Formal analysis.

### Declaration of competing interest

The authors declare that they have no known competing financial interests or personal relationships that could have appeared to influence the work reported in this paper.

### Acknowledgments

This work was supported by the Yancheng Science and Technology Bureau (grant numbers YCBK2023002), National Natural Science Foundation of China (grant numbers 52270072, 42227806), and the National Key Research and Development Program of China (grant numbers 2023YFE0100900).

### Appendix A. Supplementary data

Supplementary data to this article can be found online at <https://doi.org/10.1016/j.jenvman.2025.126657>.

### Data availability

No data was used for the research described in the article.

### References

- Bashiri, R., Irfan, M., Mohamed, N., Sufian, S., Ling, L., Suhami, N., Samsudin, M., 2021. Hierarchically  $\text{SrTiO}_3@\text{TiO}_2@\text{Fe}_2\text{O}_3$  nanorod heterostructures for enhanced photoelectrochemical water splitting. *Int. J. Hydrogen Energy* 46, 24607–24619. <https://doi.org/10.1016/j.ijhydene.2020.02.106>.
- Boynd-Shekalgourabi, S., Sharatiatnia, Z., 2024. Hexagonal mesoporous silica/perovskite oxides composites as unique scattering layers in photoelectrodes of high performance dye-sensitized photovoltaics. *Int. J. Hydrogen Energy* 51, 1397–1412. <https://doi.org/10.1016/j.ijhydene.2023.11.109>.
- Boonpai, S., Surije, K., Jongsomjit, B., Panpranon, J., Praserttham, P., 2020. Hydrogen activated  $\text{WO}_x$ -supported catalysts for lewis acid transformation to bronsted acid observed in situ DRIFTS of adsorbed ammonia: effect of different supports on the lewis acid transformation. *Catal. Today* 358, 370–386. <https://doi.org/10.1016/j.cattod.2019.06.073>.
- Cakra Wardhana, A., Yamaguchi, A., Shoji, S., Liu, M., Fujita, T., Hitosugi, T., Miyauchi, M., 2020. Visible-light-driven photocatalysis via reductant-to-band charge transfer in Cr(III) nanocluster-loaded  $\text{SrTiO}_3$  system. *Appl. Catal. B Environ.* 270, 118883. <https://doi.org/10.1016/j.apcatb.2020.118883>.
- Chen, L., Zheng, H., Li, A., Qiu, X., Wang, L., 2024. Lewis acid-rich  $\text{SrFe}_x\text{Ti}_{1-x}\text{O}_3/\text{TiO}_2$  to enhance the photocatalytic reduction of nitrate to  $\text{N}_2$ . *J. Hazard. Mater.* 473, 134634. <https://doi.org/10.1016/j.jhazmat.2024.134634>.
- da Silva, L., M'Peko, J., Andrés, J., Beltrán, A., Gracia, L., Bernardi, M., Mesquita, A., Antonelli, E., Moreira, M., Mastelaro, V., 2014. Insight into the effects of Fe addition on the local structure and electronic properties of  $\text{SrTiO}_3$ . *J. Phys. Chem. C* 118, 4930–4940. <https://doi.org/10.1021/jp408839q>.
- Drisko, G., Carretero-Genevrier, A., Perrot, A., Gich, M., Gàzquez, J., Rodriguez-Carvajal, J., Favre, L., Gross, D., Boissière, C., Sanchez, C., 2015. Crystallization of hollow mesoporous silica nanoparticles. *Chem. Commun.* 51, 4164–4167. <https://doi.org/10.1039/C4CC0782D>.
- Grabowska, E., 2016. Selected perovskite oxides: characterization, preparation and photocatalytic properties-A review. *Appl. Catal. B Environ. Energy* 186, 97–126. <https://doi.org/10.1016/j.apcatb.2015.12.035>.
- Hou, Z., Chen, F., Wang, J., François-Xavier, C., Wintgens, T., 2018. Novel  $\text{Pd}/\text{GdCrO}_3$  composite for photo-catalytic reduction of nitrate to  $\text{N}_2$  with high selectivity and activity. *Appl. Catal. B Environ. Energy* 232, 124–134. <https://doi.org/10.1016/j.apcatb.2018.03.055>.
- Hou, Z., Chu, J., Liu, C., Wang, J., Li, A., Lin, T., François-Xavier, C., 2021. High efficient photocatalytic reduction of nitrate to  $\text{N}_2$  by Core-shell  $\text{Ag/SiO}_2@\text{cTiO}_2$  with synergistic effect of light scattering and surface plasmon resonance. *Chem. Eng. J.* 415, 128863. <https://doi.org/10.1016/j.cej.2021.128863>.
- Jain, P., El-Sayed, M., 2008. Noble metal nanoparticle pairs: effect of medium for enhanced nanosensing. *Nano Lett.* 8, 4347–4352. <https://doi.org/10.1021/nl8021835>.
- Jiang, C., Zhang, M., Dong, G., Wei, T., Feng, J., Ren, Y., Luan, T., 2022. Photocatalytic nitrate reduction by a non-metal catalyst h-BN: performance and mechanism. *Chem. Eng. J.* 429, 132216. <https://doi.org/10.1016/j.cej.2021.132216>.
- Lee, S., Kim, S., Park, C., Kim, W., Ryu, S., Choi, W., 2021. Solar denitrification coupled with in situ water splitting. *Energy Environ. Sci.* 14, 4437–44509. <https://doi.org/10.1039/DIEE01342D>.
- Lei, J., Bi, W., Wang, M., Jiang, H., Hu, Y., Li, C., 2024. Efficient electron transport at the perovskite nanodots interface facilitates  $\text{CO}_2$  photoreduction. *J. Colloid Interface Sci.* 679, 420–429. <https://doi.org/10.1016/j.jcis.2024.09.179>.
- Li, C., Yi, S., Liu, Y., Niu, Z., Yue, X., Liu, Z., 2021. In-situ constructing S-scheme/schottky junction and oxygen vacancy on  $\text{SrTiO}_3$  to steer charge transfer for boosted photocatalytic  $\text{H}_2$  evolution. *Chem. Eng. J.* 417, 129231. <https://doi.org/10.1016/j.cej.2021.129231>.
- Li, X., Zhang, M., Feng, J., Bai, C., Ren, Y., 2022a. Electrostatic self-assembly to form unique  $\text{LiNbO}_3/\text{ZnS}$  core-shell structure for photocatalytic nitrate reduction enhancement. *J. Colloid Interface Sci.* 607, 1323–1332. <https://doi.org/10.1016/j.jcis.2021.09.069>.
- Li, Q., Liu, Y., Wan, Z., Cao, H., Zhang, S., Zhou, Y., Ye, X., Liu, X., Zhang, D., 2022b. Microwave-assisted synthesis of oxygen vacancy associated  $\text{TiO}_2$  for efficient photocatalytic nitrate reduction. *Chin. Chem. Lett.* 33, 3835–3841. <https://doi.org/10.1016/j.clet.2021.12.025>.
- Liu, G., You, S., Ma, M., Huang, H., Ren, N., 2016a. Removal of nitrate by photocatalytic denitrification using nonlinear optical material. *Environ. Sci. Technol.* 50, 11218–11225. <https://doi.org/10.1021/acs.est.6b03455>.
- Liu, G., You, S., Ma, M., Huang, H., Ren, N., 2016b. Removal of nitrate by photocatalytic denitrification using nonlinear optical material. *Environ. Sci. Technol.* 50, 11218–11225. <https://doi.org/10.1021/acs.est.6b03455>.
- Liu, N., Li, R., Zhu, J., Liu, Q., Chen, R., Yu, J., Li, Y., Zhang, H., Wang, J., 2023. Z-scheme heterojunction  $\text{ZnS}/\text{WO}_3$  composite: photocatalytic reduction of uranium and band gap regulation mechanism. *J. Colloid Interface Sci.* 630, 727–737. <https://doi.org/10.1016/j.jcis.2022.10.151>.
- Liu, R., Yu, Z., Zhang, R., Xiong, J., Qiao, Y., Liu, X., Lu, X., 2024. Hollow nanoreactors for controlled photocatalytic behaviors: fundamental theory, structure–performance relationship, and catalytic advantages. *Small* 20, 2308142. <https://doi.org/10.1002/smll.202308142>.
- Luo, H., Li, S., Wu, Z., Liu, Y., Luo, W., Li, W., Zhang, D., Chen, J., Yang, J., 2023. Modulating the active hydrogen adsorption on Fe-N interface for boosted electrocatalytic nitrate reduction with ultra-long stability. *Adv. Mater.* 35, 2304695. <https://doi.org/10.1002/adma.202304695>.
- Saito, K., Setoura, K., Ito, S., Miyasaka, H., Mitsuda, Y., Tatsuma, T., 2017. Plasmonic control and stabilization of asymmetric light scattering from Ag nanocubes on  $\text{TiO}_2$ . *ACS Appl. Mater. Interfaces* 9, 11064–11072. <https://doi.org/10.1021/acsmami.7b01457>.
- Shen, W., Feng, L., Feng, H., Kong, Z., Guo, M., 2011. Ultrafine silver(II) oxide particles decorated porous ceramic composites for water treatment. *Chem. Eng. J.* 175, 592–599. <https://doi.org/10.1016/j.cej.2011.09.121>.
- Shi, H., Li, C., Wang, L., Wang, W., Bian, J., Meng, X., 2022. Photocatalytic reduction of nitrate pollutants by novel Z-scheme  $\text{ZnSe/BiVO}_4$  heterostructures with high  $\text{N}_2$  selectivity. *Sep. Purif. Technol.* 300, 121854. <https://doi.org/10.1016/j.seppur.2022.121854>.
- Son, S., Hwang, S., Kim, C., Yun, J., Jang, J., 2013. Designed synthesis of  $\text{SiO}_2/\text{TiO}_2$  core/shell structure as light scattering material for highly efficient dye-sensitized solar cells. *ACS Appl. Mater. Interfaces* 5, 4815–4820. <https://doi.org/10.1021/am400441v>.
- Sulaiman, M., Mustafa and Y., 2021. Review on the effect of compact layers and light scattering layers on the enhancement of dye-sensitized solar cells. *Sol. Energy* 215, 26–43. <https://doi.org/10.1016/j.solener.2020.12.030>.
- Tang, C., Zhu, J., Zhou, Q., Wei, J., Zhu, R., He, H., 2014. Surface heterogeneity of  $\text{SiO}_2$  polymorphs: an XPS investigation of  $\alpha$ -quartz and  $\alpha$ -cristobalite. *J. Phys. Chem. C* 118, 26249–26257. <https://doi.org/10.1021/jp509338x>.
- Tang, P., Tang, W., Lyu, S., Brusseau, M., Xue, Y., Xue, Z., Xue, Q., 2019. Mechanism of carbon tetrachloride reduction in ferrous ion activated calcium peroxide system in the presence of methanol. *Chem. Eng. J.* 362, 243–250. <https://doi.org/10.1016/j.cej.2019.01.034>.
- Tong, Z., Yang, D., Li, Z., Nan, Y., Ding, F., Shen, Y., Jiang, Z., 2017. Thylakoid-inspired multishell  $\text{g-C}_3\text{N}_4$  nanocapsules with enhanced visible-light harvesting and electron transfer properties for high-efficiency photocatalysis. *ACS Nano* 11, 1103–1112. <https://doi.org/10.1021/acsnano.6b08251>.
- Wang, L., Cheng, B., Zhang, L., Yu, J., 2021. In situ irradiated XPS investigation on S-scheme  $\text{TiO}_2@\text{ZnIn}_2\text{S}_4$  photocatalyst for efficient photocatalytic  $\text{CO}_2$  reduction. *Small* 17, 2103447. <https://doi.org/10.1002/smll.202103447>.

- Wu, Q., Zheng, Q., van de Krol, R., 2012. Creating oxygen vacancies as a novel strategy to form tetrahedrally coordinated  $Ti^{4+}$  in Fe/TiO<sub>2</sub> nanoparticles. *J. Phys. Chem. C* 116, 7219–7226. <https://doi.org/10.1021/jp212577g>.
- Xiao, M., Wang, Z., Lyu, M., Luo, B., Wang, S., Liu, G., Cheng, H., Wang, L., 2019. Hollow nanostructures for photocatalysis: advantages and challenges. *Adv. Mater.* 31, 1801369. <https://doi.org/10.1002/adma.201801369>.
- Xie, T., Sun, X., Lin, J., 2008. Enhanced photocatalytic degradation of RhB driven by visible light-induced MMCT of Ti(IV)-O-Fe(II) formed in Fe-doped SrTiO<sub>3</sub>. *J. Phys. Chem. C* 112, 9753–9759. <https://doi.org/10.1021/jp711797a>.
- Xu, Q., Zhang, L., Cheng, B., Fan, J., Yu, J., 2020. S-Scheme heterojunction photocatalyst. *Chem* 6, 1543–1559. <https://doi.org/10.1016/j.chempr.2020.06.010>.
- Xu, Z., Xu, L., Yang, R., Zhou, Z., Zeng, G., Lyu, S., 2023. Mechanistic insights into surfactant in enhanced reductive degradation of perchlorinated organic contaminants in fenton system. *Sep. Purif. Technol.* 322, 124220. <https://doi.org/10.1016/j.seppur.2023.124220>.
- Yang, W., Wang, J., Chen, R., Xiao, L., Shen, S., Li, J., Dong, F., 2022. Reaction mechanism and selectivity regulation of photocatalytic nitrate reduction for wastewater purification: progress and challenges. *J. Mater. Chem. A* 10, 17357. <https://doi.org/10.1039/D2TA04611C>, 11376.
- Yang, Y., Sun, Y., Lu, G., Gao, W., Yang, T., 2024. From lewis acid to lewis base by La<sup>3+</sup> to Y<sup>3+</sup> substitution in  $\alpha$ -YBaO<sub>6</sub>: local structure modification induced lewis basicity. *J. Phys. Chem. Lett.* 15, 3554–3558. <https://doi.org/10.1021/acs.jpclett.4c00234>.
- Yu, S., Shen, S., Zhang, C., Chen, R., Dan, H., Li, J., Dong, F., 2024. Accelerating the production of formate radicals for nitrate purification via a redox-regulated photocatalysis route. *Appl. Catal. B Environ. Energy* 358, 124419. <https://doi.org/10.1016/j.apcatb.2024.124419>.
- Yuan, D., Li, X., Zhao, Q., 2013. Preparation and characterization of Ni-Ti-O mixed oxide for selective catalytic reduction of NO under lean-burn conditions. *Chin. J. Catal.* 34, 1449–1455. [https://doi.org/10.1016/S1872-2067\(12\)60614-7](https://doi.org/10.1016/S1872-2067(12)60614-7).
- Zhang, Y., Liu, C., Zhou, Y., Wang, J., Li, A., 2023. Boosting light harvesting and charge separation over hollow double-shelled Ag@SrTiO<sub>3</sub>-TiO<sub>2</sub> with Z-scheme heterostructure for highly efficient photocatalytic reduction of nitrate to N<sub>2</sub>. *Chem. Eng. J.* 457, 140992. <https://doi.org/10.1016/j.cej.2022.140992>.
- Zhao, J., Li, N., Yu, R., Zhao, Z., Nan, J., 2018. Magnetic field enhanced denitrification in nitrate and ammonia contaminated water under 3D/2D Mn<sub>2</sub>O<sub>3</sub>-g-C<sub>3</sub>N<sub>4</sub> photocatalysis. *Chem. Eng. J.* 349, 530–538. <https://doi.org/10.1016/j.cej.2018.05.124>.
- Zhou, X., Zhang, C., Li, Y., 2021. Time-delayed photocatalysis enhanced microbial nitrate reduction via solar energy storage in carbon nitrides. *Chem. Eng. J.* 417, 127904. <https://doi.org/10.1016/j.cej.2020.127904>.